RSC Advances

PAPER

View Article Online
View Journal | View Issue

Cite this: *RSC Adv.*, 2025, **15**, 27356

Graphene oxide – polymer nanocomposites for efficient water hardness removal: a step towards healthier drinking water†

P. H. P. Panapitiya,[a] Tharindra Weerakoon,[a] M. Shanika Fernando,[a] A. K. D. V. K. Wimalasiri,[a] K. M. Nalin de Silva *[a] and Rohini M. de Silva *[ab]

A new, non-toxic, environmentally friendly nanocomposite, based on graphene oxide and biopolymers was developed as an effective adsorbent for water hardness removal. Graphene oxide was synthesized by a modified Hummers' method, whereas crosslinked carboxymethyl cellulose (CMC) and chitosan were used as biopolymers. Montmorillonite (MMT) was utilized as an additive to enhance the adsorbent's performance. The solubility and adsorption behaviours of the prepared materials were investigated in respect to calcium ions (Ca^{2+}) and magnesium ions (Mg^{2+}). Among the prepared materials, a film containing graphene oxide (GO), crosslinked carboxymethyl cellulose (CMC), and montmorillonite (MMT), denoted as GO-CMC-MMT-3, exhibited the highest water softening capacity. The successful synthesis of the materials was confirmed through scanning electron microscopy (SEM), Fourier-transform infrared spectroscopy (FT-IR), X-ray diffraction (XRD), and ultraviolet-visible spectroscopy (UV-Vis). The optimal pH for the adsorption process was around 6–7. Kinetic studies showed that second-order kinetic model described the adsorption process. The thermodynamic analysis indicated that the process was endothermic in nature and showed a reduced degree of spontaneity at the given conditions. The Langmuir isotherm model was the best fit, and the adsorption capacities were 6.46 mg g^{-1} for Mg^{2+} and 7.98 mg g^{-1} for Ca^{2+}, which indicated the formation of a monolayer of cations on homogeneous adsorption sites. Further, an investigation on the reusability of gravity filtration was carried out, demonstrating the practical utility of the GO-CMC-MMT-3 membrane in real-life water treatment.

Received 23rd January 2025
Accepted 17th June 2025

DOI: 10.1039/d5ra00562k

rsc.li/rsc-advances

1 Introduction

The lack of access to clean drinking water is a pressing global issue, particularly impacting populations in developing countries. This crisis is largely driven by the contamination of water bodies with pollutants such as heavy metal ions, agrochemicals, and various organic and inorganic substances introduced through human activities. Additionally, the presence of high mineral content in water, prevalent in many regions worldwide, exacerbates the problem by contributing to water hardness, a significant water quality concern.

Water hardness is primarily determined by the concentrations of dissolved calcium (Ca^{2+}) and magnesium (Mg^{2+}) ions. The issues caused by water hardness range from an unpleasant taste to excessive mineral scaling, which obstructs water flow in pipes, damages equipment such as boilers, and shortens the lifespan of fabrics. Additionally, it reduces soap's effectiveness by forming soap scum through the complexation of metal ions with soap molecules.

Hard and very hard water, with Ca^{2+} and Mg^{2+} levels of 120 ppm or above can significantly impact on human health. Although the body can regulate the absorption of these ions in the intestine up to a certain level, excessive intake will cause serious health complications.[1] In Sri Lanka, the chronic kidney disease of unknown etiology (CKDu) is attributed to various chemical factors related to water hardness.[2,3] Studies have shown a strong correlation between the geographical distribution of CKDu patients and the areas with high ground water hardness, where as 96% of CKDu patients reside in areas with hard or very hard water.[4] Due to these risk factors associated with water hardness, it is recommended to soften the water before consumption. Various methods are applied on both industrial and domestic scales to achieve water softening.

The temporary hardness of water can easily be removed through methods like, boiling, adding slaked lime (Clark's method),[5] or using washing soda.[6] However, the permanent hardness requires more advanced methods such as Gan's permutate method,[7] Calgon's process, carbonation,[8] electrocoagulation,[9] capacitive deionization (CDI),[10] electrolysis,[11] use

[a]*Centre for Advanced Materials and Devices (CAMD), Department of Chemistry, University of Colombo, Colombo 03, Sri Lanka. E-mail: rohini@chem.cmb.ac.lk*
[b]*Department of Life Sciences, Faculty of Science, NSBM Green University, Mahenwatta, Pitipana, Homagama 10206, Sri Lanka*

† Electronic supplementary information (ESI) available. See DOI: https://doi.org/10.1039/d5ra00562k

of ion exchange resins,[12,13] ultrasounds with ion exchange,[14] precipitation using pellet reactor,[15] membrane separation systems, nanofiltration membranes,[16] freezing with dry gas,[17] electrodialysis,[18] electro deionization(EDI),[19] and various adsorption methods.[20,21] Among these techniques, absorption stands out due to its simplicity and cost effectiveness, which can be applicable at both industrial and domestic scales, making it the focus of interest in this study.

According to the literature different materials have been studied as absorbents. Some of them are activated carbon,[22,23] different lignocellulose materials,[24,25] plant-based ashes,[26] synthetic and derived natural compounds,[27,28] synthetic and natural zeolites,[29,30] clay-based materials,[31] polymer-based materials,[27] and ion exchange resins.[32,33] Nanomaterials such as carbon nanotubes,[34] graphene-based materials[35] have also been given significant attention as adsorbents due to their high absorption efficiency. However, concerns about high cost and toxicity, make nanomaterials less favourable. As a result, this study mainly focuses nanocomposite, which offers advantages like enhanced adsorption and mechanical properties, cost reduction, high characterization potential, and minimized toxicity concerns. Among nanocomposites, biopolymer-based materials have given a considerable interest in water purification, particularly bio nanocomposites (nanocomposites consist of biopolymers) due to their non-toxicity,[36,37] excellent chelation properties and biodegradability.[38,39]

According to Dimiev *et al.* (2013) and Lakshmi *et al.* (2017), graphene-based nanocomposites have shown an excellent adsorption capacity toward a wide range of contaminants,[40] and also water hardness.[41,42] Carboxymethyl cellulose (CMC) and chitosan have also been widely investigated for water purification due to their biocompatibility, abundance, and high chelating properties.[5,43–46] However, there is a lack of well-rounded exploration of the effectiveness of bio-nanocomposites on the removal of water hardness. Hence, this study will help to examine their potential in improving the adsorption of Ca^{2+} and Mg^{2+} ions. Furthermore, cross-linking of the biopolymer CMC with citric acid and glycerol were studied as these components are simple, cheap, and non-toxic cross-linking agents. This approach is expected to improve the characteristics of the composite, including its negative charge, mechanical strength, antifouling properties, chelation ability toward negatively charged groups, cation exchange capacity, and ability to entrap MMT clay and GO layer particles.[41]

The layers of MMT are held together mainly by van der Waals forces and electrostatic interactions. The intercalation of the MMT layers is readily attained with different polymers by means of isomorphous substitution, which imparts a negative charge on adjacent oxygen atoms. This negative charge enhances the ability of the clay to attract positively charged molecules and cations. With its high surface area, excellent mechanical stability, and notable swelling capacity, this polymer demonstrates superior adsorption properties and high cation exchangeability.[47,48]

This work was mainly focused on developing an effective biopolymer nanocomposite that can be used to remove water hardness by the adsorption of Ca^{2+} and Mg^{2+} ions *via* different interactions. In this research, melt intercalation/melt mixing process is used to form the nanocomposite which is more compatible with industrial polymer process.[49,50] For this study, GO was taken as the nanomaterial and it was synthesized using Sri Lankan vein graphite which is known as the best graphite in the world.

2 Materials and methods

2.1 Materials

All chemicals used were of analytical reagent grade. Graphite powder (Bogala vein graphite), sulphuric acid (H_2SO_4) (assay – 98%), potassium permanganate ($KMnO_4$) (assay – 99.5%), montmorillonite K 10 (surface area 220–270 $m^2\ g^{-1}$), hydrogen peroxide (H_2O_2) (30%), magnesium nitrate hexahydrate ($Mg(NO_3)_2 \cdot 6H_2O$) (assay – 98%), calcium chloride dihydrate ($CaCl \cdot 2H_2O$) (assay – 99.5%), carboxymethyl cellulose (CMC) (Average M. W 90 000 g mol^{-1}), chitosan (low molecular weight), acetic acid (CH_3COOH) (assay – 99.8%), hydrochloric acid (HCl) (assay – 96%), glycerol ($C_3H_8O_3$) (assay – 98.5%), citric acid anhydrous ($C_6H_8O_7$) (assay – 99.5%) were purchased from SIGMA-ALDRICH, Germany. The distilled water was produced in the laboratory.

2.2 Synthesis of graphene oxide

Graphene oxide (GO) was synthesized using the modified hummers method with the some minor changes as explained in the ESI (S1).†[51,52]

2.3 Preparation of cross-linked carboxymethyl cellulose (CMC)

Cross-linked carboxymethyl cellulose was prepared by adding CMC powder (5.00 g) to 200 ml beaker along with distilled water (100 ml, 80 °C). Citric acid (1.20 g) and glycerol (3.80 g) was added to CMC solution (0.05% W/V). After the addition, the temperature of the solution was maintained at 100 °C for 30 minutes. Then the temperature in the slurry was further increased up to 180 °C and maintained for 1 hour under continuous stirring. The resulted solution was quickly poured into Petri dishes and incubated overnight at 60 °C in an oven (HERAEUS UT 6060). Resulted cross-linked CMC membranes were separated from Petri dishes and stored in a desiccator.

2.4 Preparation of GO-CMC membranes

A liquid form of cross-linked CMC (100 ml) was prepared according to section 2.3 and allowed to reduce the temperature below 100 °C. (Not less than 80 °C) then 0.36 g of prepared GO was added in to a liquid form of cross-linked CMC and stirred for about 1 hour until result a homogenous mixture. The mixture was poured into 6 Petri plates and kept overnight in the oven at 60 °C. Then the formed membranes were removed and stored in a desiccator. The process was repeated with high GO concentration (1.0 g) to make different GO to CMC ratio.

2.5 Formation of GO-MMT beads

A mass of MMT powder (1.00 g) and distilled water (10 ml) were added into a beaker and stirred for one hour at 100 °C. After 24 hours of incubation period at room temperature, the mixture was stirred again for 3 hours at 100 °C to make a dispersion of MMT. Then GO (0.3 g) was added into the mixture and stirred for another 2 hours and kept in the oven at 100 °C for 2 hours. Small composite beads were prepared, and the beads were dried at 100 °C for 4 hours and stored in a desiccator.

2.6 Formation of GO-CMC-MMT membranes

Solutions of 100 ml of cross-linked CMC were prepared into three beakers according to the above-mentioned procedure. MMT dispersions (According to section 2.5) of 1.7%, 3.3% and 5% (W/V) were prepared and mixed with CMC solutions. Then 0.36 g of GO portions were added into each mixture. The mixtures were stirred well. The three mixtures were labelled as GO-CMC-MMT-1(1.7% of MMT), GO-CMC-MMT-2 (3.3% g of MMT), and GO-CMC-MMT-3 (5.0% of MMT) membranes. Each mixture was poured into Petri plates and kept in the oven at 60 °C for 5 hours. Then the mixtures were placed at room temperature for one day. All three prepared membranes were removed and stored in the desiccator.

2.7 Preparation of CMC-MMT membrane

A liquid form of cross-linked CMC (100 ml) was prepared in a beaker as above-mentioned procedure and allowed to reduce the temperature lower than 80 °C. Then 50 ml portion of MMT dispersion (5.0% of MMT) was added into CMC solution and mixed. Then the formed mixture was poured into Petri plates and kept overnight in the oven at 60 °C. The resulted membrane was separated and stored in a desiccator.

2.8 Preparation of GO-chitosan membrane

Commercially available chitosan powder (1.00 g) was added to a 200 ml beaker along with 100 ml of distilled water which was at 100 °C and the mixture was stirred using a magnetic stirrer. After complete dissolution, acetic acid (1 mol dm^{-3}, 2.0 ml) was added to the solution. The temperature of the solution was maintained at 100 °C for 30 minutes under continuous stirring. This hot solution of chitosan was allowed to cool down (lower than 100 °C). Then GO (0.36 g) was added into chitosan solution and stirred well. The mixture was poured into Petri plates and kept overnight in the oven at 60 °C. Resulted membranes were removed and stored in a desiccator.

2.9 Identification of the best materials for Mg^{2+} and Ca^{2+} adsorption

Out of all the synthesized materials, the best material to be used as adsorbent for water hardness was identified by considering several factors like solubility (S2.1), contact time (S2.2) and the adsorption capacities (S2.2) of Ca^{2+} and Mg^{2+} ions over time. The detailed procedures for the selection of the best material are given in ESI (S2).†

2.10 Characterization of the best synthesized materials

Various techniques were employed throughout this research to characterize cross-linked CMC, graphene oxide, and the resulting nanocomposite. Even though CMC polymer and montmorillonite (MMT) clay are already utilized for commercial purposes, only a limited number of characterization techniques have been applied to them. When characterizing synthesized GO, UV-VISIBLE Spectrometer (GENESYS 10S) and Fourier transform infrared spectroscopy (FT-IR, PerkinElmer spectrum two 95 033) were used. To investigate the crystalline nature of the GO, X-ray diffractogram (XRD, Rigaku model-smart lab SE) was used. Scanning electron microscope (SEM, model ZEISS EVO 18) was used to visualize the layered structure.

The initial comparative adsorption studies indicated that GO-CMC-MMT-3 membrane is the best material for the removal of Ca^{2+} and Mg^{2+} from water. After the formation of nanocomposite, SEM images, FT-IR data, and XRD data was used to determine the intercalation and alternations of GO in crossliked CMC matrix. FT-IR analysis was also performed for pure CMC powder, MMT powder, and crosslinked CMC membrane in the wavelength range between 400 cm^{-1} and 4000 cm^{-1}. The XRD analysis was performed using Cu-Kα radiation over a 2θ range of 2–80°, with a step size of 0.02° for crosslinked CMC membrane, GO-CMC-MMT-3 before and after the adsorption Ca^{2+} and Mg^{2+} cations. The SEM analysis was performed with 10.00 KV voltage and 5.00 KX, 25.00 KX magnifications.

2.11 Batch adsorption studies for GO-CMC-MMT-3 membrane

2.11.1 The effect of pH on GO-CMC-MMT-3 membrane. Ca^{2+} and Mg^{2+} solutions (10 ppm, 50 ml) with different pH values (2 pH to 8 pH) were prepared by adding 0.1 mol dm^{-3} HCl and 0.5 mol dm^{-3} NaOH solutions. Each solution was divided into 2 portions (25 ml for each). GO-CMC-MMT-3 membrane (0.0500 g) was added to one portion of each pH value. Both the portions (membranes added containers and not added containers) were kept in the shaker for 45 minutes at 180 rpm in room temperature. Then the concentration of Mg^{2+} and Ca^{2+} in each solution were measured by MP-AES instrument and adsorption percentages were calculated. The graph of the percentage of adsorption *versus* pH was plotted.

2.11.2 Adsorption isotherm studies. The batch adsorption isotherm studies were conducted using Ca^{2+} and Mg^{2+} solutions (0.05 g, 50.0 ml) with a gradient of 10 ppm – 60 ppm concentrations. The pH of the solutions was adjusted to the optimum value (6 pH-7 pH). The solutions were shaken at 180 rpm at 30 °C for 45 minutes. This data was used for plotting the adsorption isotherms.[53] The results were fitted into the Langmuir adsorption isotherm model which is represented by its linear equation in eqn (1) also fitted into the Freundlich adsorption isotherm model which is given by its linear equation in eqn (2).

Langmuir adsorption isotherm

$$\frac{C_e}{Q_e} = \frac{1}{Q_0 K_L} + \frac{C_e}{Q_0} \quad (1)$$

Freundlich adsorption isotherm

$$\log \quad Q_e = \log \quad K_f + n \quad \log \quad C_e \tag{2}$$

where, Q_e = the amount of adsorbate on the adsorbent at equilibrium(mg l^{-1}), C_e = the equilibrium concentration of the adsorbate (mg g^{-1}), K_f = Freundlich isotherm constant, n = adsorption intensity, Q_0 = maximum molecular coverage capacity (mg g^{-1}), K_L = Langmuir isotherm constant (l ms^{-1}).

2.11.3 Effect of temperature (kinetic and thermodynamic study) of the solutions on the GO-CMC-MMT-3 membrane. The Ca^{2+} and Mg^{2+} solutions (10 ppm, 6 solutions from each) were prepared separately by using the stock solution. The pH of the solutions were set to the optimum value. After adding 0.05 g of GO-CMC-MMT-3 membrane to each container, it was shaken at different temperatures (20 °C, 30 °C, 40 °C, 60 °C) at 180 rpm. After the shaking process, the solutions were filtered using filter papers and performed the MP-AES analysis. From the results of the analysis, the plots of two kinetic models, that are linearized Lagergren – first order model in the eqn (3) and linearized Ho's pseudo – second order model in the eqn (4) were plotted.

$$\ln \quad (q_e - q_t) = \ln \quad q_e + k_1 t \ldots \tag{3}$$

$$\frac{t}{q_t} = \frac{1}{K q_e^2} + \frac{1}{q_e} t \tag{4}$$

with the use of Arrhenius equation (eqn (5)–(9)), the thermodynamic parameters, such as apparent activation energy (E_a), heat of enthalpy (ΔH), entropy change (ΔS), Gibbs free energy (ΔG) can be calculated. These results help to study the dependence of the rate on the temperature, spontaneity, and the feasibility of the adsorption process.

$$\ln k_{ap} = \ln A - \frac{E_a}{RT} \ldots \tag{5}$$

$$\Delta G^\circ = -RT \quad \ln \quad k_d \tag{6}$$

$$k_d = \frac{q_e}{c_e} \tag{7}$$

$$\Delta G^\circ = \Delta H^\circ - T\Delta S^\circ \tag{8}$$

$$\ln k_d = -\frac{\Delta H^\circ}{RT} + \frac{\Delta S^\circ}{R} \ldots \tag{9}$$

K_{ap} = apparent rate constant, A = frequency factor, E_a = activation energy, K_d = thermodynamic distribution coefficient, q_e = amount of adsorbate adsorbed on the composite at equilibrium, C_e = equilibrium concentration of adsorbate in solution, T = temperature in kelvin, R = universal gas constant.[54]

2.11.4 Reusability studies. The membrane GO-CMC-MMT-3, which showed the best properties was selected for reusability studies. A 0.10 g portion of membrane was added into Ca^{2+} (20 ppm, 30 ml) and Mg^{2+} (15 ppm, 30 ml) containing solution. Then the solution along with the membrane was shaken for 45 minutes. Then the final concentration of the solution was determined using the MP-AES. After MP-AES analysis, membrane was again shaken with 0.1 mol dm^{-3} HCl solution for 2 hours. Then the membrane was removed from the HCl solution and additional moisture was removed from the membrane by keeping in the oven at 60 °C. Once the membrane was fully dried, it was soaked again in a new Ca^{2+} (20 ppm, 30 ml) and Mg^{2+} (15 ppm, 30 ml) solution and shaken for 45 minutes. The same procedure was repeated for 4 times. Using the adsorption data, the adsorption capacity and adsorption percentages were calculated. From those results, the graph of final concentration *versus* the number of turns (uses) was plotted.

2.11.5 Gravity-filtration studies for the GO-CMC-MMT-3 membrane for original and lab water samples. Two gravity columns were set up using 0.10 g of membrane. The cotton plug was used to retain the membrane particles without getting discharge from the column. Then the original well water sample (100 ml) and prepared lab water samples (10 ppm of Mg^{2+} and Ca^{2+}) were added into the gravity columns separately. Then 10 ml fractions of the filtrate were collected into small containers. The ion concentration of each fraction and ion concentration of initial samples were determined by the MP-AES instrument. The graph of final concentration *vs.* fraction number was plotted.

3 Results and discussion

3.1 Characterization of graphene oxide

In this work GO was synthesized using a modified hummers method and characterization of synthesized GO was carried out to confirm the successful synthesis (Fig. S2†). The FT – IR spectra of aqueous GO samples (Fig. 1a) show a broad stretching peak at 3250–3350 cm^{-1} region due to higher concentration of –OH in the water and GO materials.

The other form of GO was prepared as a membrane, and its FT-IR spectrum is given in Fig. 1(b). The reduced peak size in the spectrum indicates the less water content in the membrane after drying in the vacuum oven. The peaks due to carbonyl stretching (1700–1750 cm^{-1}) and double bond stretching in graphene structure (1600–1650 cm^{-1}) also can be seen in the spectrum.[55] The broad peak at 1630 cm^{-1} in Fig. 1 a results due to overlapping of peaks in aqueous GO. The small peaks around 1000–1200 cm^{-1} in Fig. 1(b) are attributed to epoxy groups in

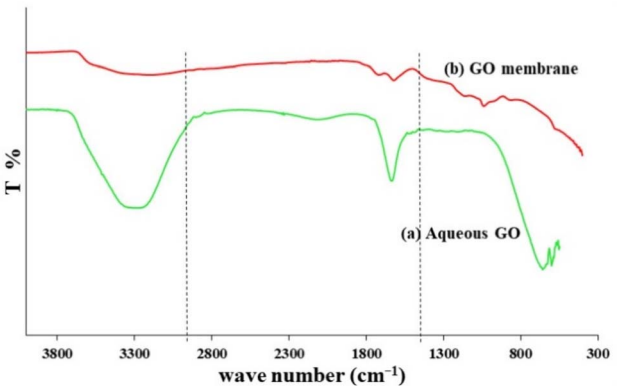

Fig. 1 The FT – IR spectrum of (a) Aqueous GO sample, (b) GO membrane; solid GO membrane formed by using vacuum oven.

the membrane which are not clearly visible in 1(a).[55] The overlapping of the peaks in the fingerprint region (400–1500 cm^{-1}) make it difficult to identify individual peaks.

The XRD spectrum was taken in the range of 2θ from 2° to 80°. This XRD spectrum (Fig. 2) of the thin layer of GO shows a sharp peak at 2θ around 9.5° and also there is a small peak at 2θ around 19°. According to the literature, the GO shows its (002) diffraction at the $2\theta = 9.70°$. Reduced graphene Oxide (rGO) shows its (002) diffraction at $2\theta = 23.7°$, graphite powder and graphene show its (002) diffraction at $2\theta = 26°$.[55,56]

In this study, graphite powder was used as the starting material. Therefore the XRD of Graphite has two characteristic peaks at $2\theta = 26°$ (002) and $2\theta = 55°$ (004)[57] and the resulted XRD spectrum of GO sample shows two peaks at the position of $2\theta = 9.5°$ (002) and $2\theta = 19°$. The d space was calculated using Bragg's law equation, $n\lambda = 2d \sin \theta$ where n is an integer for constructive interferences, λ = wavelength of the x rays, d = spacing between layers of atoms and θ = angle between the incident rays and the surface of the crystal. The calculated values were tabulated in the (Table S1†). According to the inter layer spacing values of products and reactants, it can be concluded that $2\theta = 19°$ peak appears due to GO sheets that are not fully exfoliated to GO.

After oxidation, the characteristic peaks of graphite were shifted from 26° to 9.5° indicating an increase of inter planer distance of graphene sheets. This serves as strong evidence for formation of GO. Also, the absence of characteristic peaks of graphite and graphene in the spectrum suggests that their presence is negligible in the sample.

GO samples were used in diluted concentrations in UV-visible spectrometry, as high concentrations can lead to scattering of the radiation. According to UV-visible spectrum (Fig. 3), peak at 300 nm can be attributed to $n - \pi^*$ transition of the carbonyl carbon. The expected peak that is correspond to $\pi - \pi^*$ transition of the double bond between carbon atoms is absent in the spectrum.[55]

Following the oxidation, 3.00 g of graphite, produced a total of 5.06 g of GO. However, according to the literature, 15–25% of water can be trapped even after the oven drying process. Therefore, the real value of GO can be slightly lower than that of the reported value.

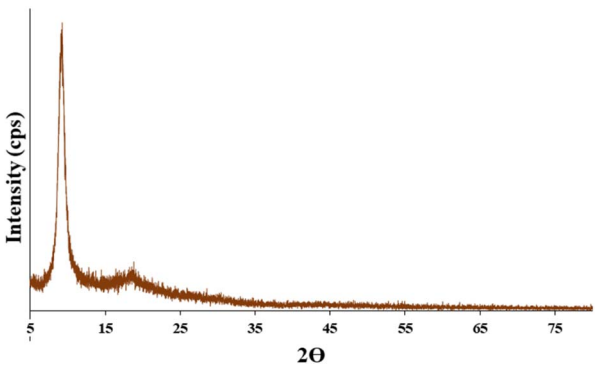

Fig. 2 The XRD spectrum of GO membrane formed by using vacuum oven.

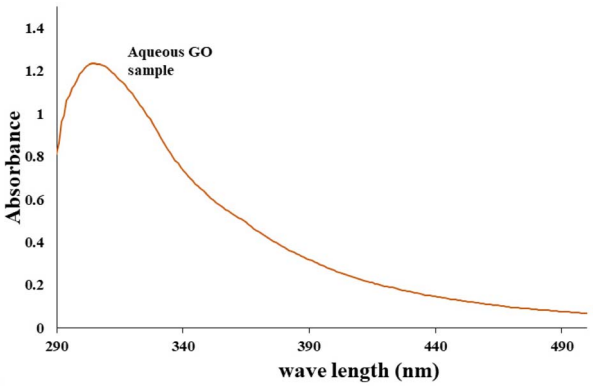

Fig. 3 The UV – VISIBLE spectrum of Aqueous GO sample.

3.2 Characterization of cross-linked CMC membrane

In the preparation of carboxymethyl cellulose (CMC), citric acid was used as a cross-linking agent, while glycerol acted as a plasticizer. The presence of carboxyl groups in citric acid makes it easy to form cross-links, increasing the negative charge of the CMC. The increased negative charge contributes to the improvement in the overall charge of the composite, which might increase its cation exchange efficiency. Simultaneously, this mechanism allows for the encapsulation of clay particles, including montmorillonite, and graphene oxide to improve the mechanical strength of a composite material. Moreover, cross-linked CMC enhances resistance to fungal attack, contributing to a cheap and sustainable material.

To remove water molecules formed during crosslinking process, the initial solution was heated to 180 °C and graphene oxide was added only after the crosslinks had formed. To avoid the disturbance of the GO structure, the solution was allowed to cool down to about 100 °C before introducing the GO. According to the FT-IR spectrum (Fig. 4b) of CMC powder, there is a wide absorption peak between 3000–3400 cm^{-1} due to stretching vibrations of – OH groups. Peak at 2900 cm^{-1} is correspond to CH_2– stretching vibrations, and peak at 1590 cm^{-1} is due to stretching vibrations of carbonyl groups (–COO–). Also, the peaks at 1420 cm^{-1}, 1325 cm^{-1}, and 1050 cm^{-1} can be attributed to –CH_2– scissoring, –OH bending, and –C–O–C– stretching frequencies respectively.[58]

Peaks at 3000 cm^{-1}, 3400 cm^{-1} and 2900 cm^{-1} were almost unchanged after the crosslink formation, while absorbance values were increased compared to CMC powder. That may be due to increased concentration of –OH groups and –CH_2- (Fig. 4a). And also due to the stretching vibrations of protonated carboxyl groups in citric acid, a novel peak at 1718 cm^{-1} was visible apart from the peak at 1590 cm^{-1} which is due to the stretching vibrations of carbonyl groups. Peaks at 1408 cm^{-1} and 1320 cm^{-1} are correspond to –CH_2– scissoring and –OH bending vibrations respectively. Peak at 1220 cm^{-1} can be due to –C–OH groups on the citric acid units.

Peak at 1050 cm^{-1} in CMC powder has been split into three peaks as at 1100 cm^{-1} (due to –O–C– stretching) 1033 cm^{-1}, and 919 cm^{-1} (due to –C–O–C– stretching) in cross linked CMC

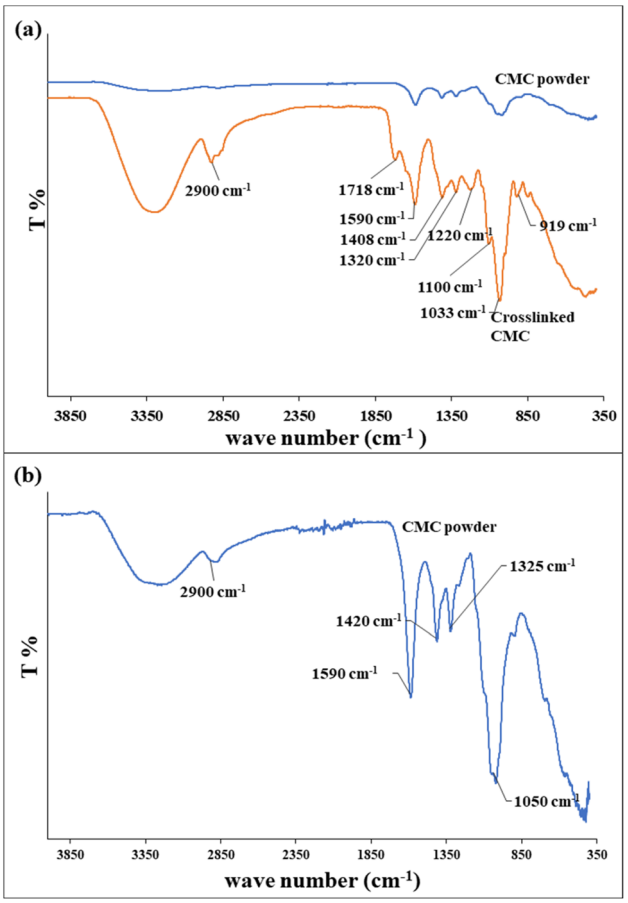

Fig. 4 The FT – IR spectrum of (a) cross-linked CMC and CMC powder, (b) the expanded FT- IR spectrum of CMC powder.

spectrum and these peaks have been shifted from the original position, mainly due to the stability of H bonds formed in the polysaccharide molecules.[58,59] Based on the above data, high efficiency of cross link formation can be observed.[1]

3.3 Identification of the optimum membrane

In order to identify the optimum membrane, different GO based nanocomposites were tested with cross linked CMC and MMT. Among them best composition was GO-CMC-MMT-3 membrane depending on its solubility and adsorption capacity over the time as given in ESI (S4).† Therefore, further studies were carried out on GO-CMC-MMT-3 membrane (Fig. 5).

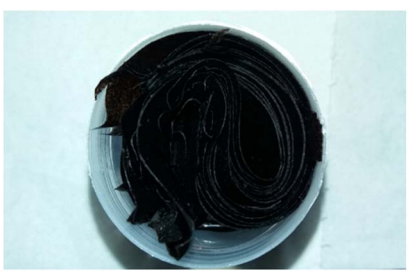

Fig. 5 Prepared GO-CMC-MMT-3 membrane type nanocomposite.

The results of the solubility studies and comparative adsorption studies are provided and explained in the ESI using Tables S2, S3,† and Fig. 6.[60,61]

According to the results, the adsorption percentage of Ca^{2+} ion is comparatively higher in the membrane than that of Mg^{2+} ion. This can be explained by the hydration of metal ions in aqueous solutions and hydration effect of the membrane functional groups. In aqueous solutions, the metal ions are existing as hydrated ions in which the metal ions are surrounded by H_2O molecules. This occurs due to dipole–dipole interactions between the positive charge metal ion and the negative charge oxygen atom in the H_2O molecules. These H_2O molecules form a structured shell around the metal ion.

The Mg^{2+} which has the higher charge density compared to Ca^{2+}, forms a larger hydration shell due to strong interactions between water molecules and metal ions and conversely, larger metal ions with low charge density like Ca^{2+} have smaller hydration shells due to weak interactions between water molecules and metal ions. Because of these weak interactions, during shaking, weak shells with weak interactions undergo rearrangements or loss partially or completely. The metals ions with lower charge density easily undergo these rearrangements and lost its hydration shell. This will lead to a difference in ion selectivity in the same membrane. When considering Ca^{2+} and

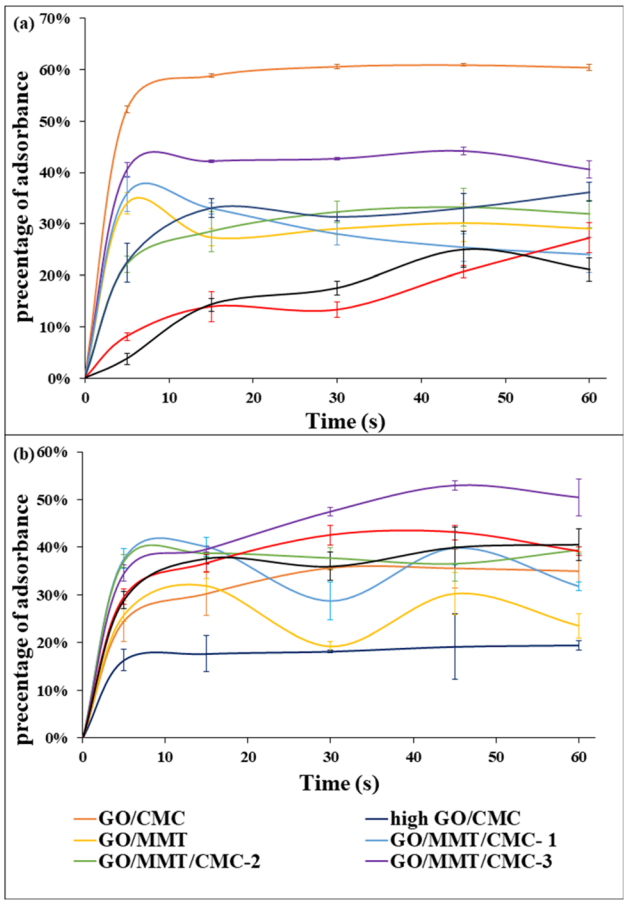

Fig. 6 (a) The graph of percentage of adsorption of Ca^{2+}, (b) the graph of percentage of adsorption of Mg^{2+}.

Mg^{2+} ions, the ionic radius of Ca^{2+} is larger than that of Mg^{2+}. Therefore, the Mg^{2+} has a strong and larger hydration shell and Ca^{2+} has a soft and smaller hydration shell which leads to higher interactions between Ca^{2+} and negative charge on the membrane compared to Mg^{2+}.[38] Adsorption properties are also affected by the hydration effect of the membrane functional groups. Once the functional groups on the membrane which have the higher negative charge, interact with the positive polarity of the water molecules, membrane gets hydrated and the affinity of membrane for strongly hydrated cations such as Mg^{2+} get decrease and less hydrated cations interactions increase due to electrostatic interactions.[38]

During the competitive uptake of Ca^{2+} and Mg^{2+} ions from an aqueous solution, the membrane should exhibit simultaneous adsorption behaviour for both ions.[62] But according to the results, Ca^{2+} ions in GO-CMC membrane gives highest adsorption percentage (61.50%) with in a contact time of 60 minutes (Table S3† and Fig. 6) while Mg^{2+} ions give the highest adsorption capacity of 53.00% in contact time of 45 minutes. When evaluating the adsorption percentages of both Ca^{2+} and Mg^{2+}, GO-CMC-MMT-3 emerges as the most effective material, achieving the highest removal percentage of total hardness. Consequently, this material was deemed the best and subjected to further adsorption studies.

This membrane specifically includes 2.50 g of MMT clay in addition to CMC and GO. During the formation of nanocomposite membranes, three membranes containing varying amounts of MMT were produced. It was observed, by increasing the amount of MMT enhanced Mg^{2+} adsorption; however, exceeding 2.50 g of MMT caused the membrane to dissolve in water. This is because each layer consists of two types of structural sheets: octahedral and tetrahedral. The tetrahedral sheets are composed of silicon–oxygen tetrahedra, while the octahedral sheets are situated between two tetrahedral sheets. The octahedral structure is formed by aluminium or magnesium ions in six-fold coordination with oxygen atoms and hydroxyl groups from the adjacent tetrahedral sheets. Multiple layers in the MMT clay are held together by weak van der Waals forces or interlayer cations.[63]

Isomorphous substitution of clay mineral generates a charge. In this process, silicon in the tetrahedral coordination places, replace by aluminium, as aluminium is small enough to fit into these sites. Similarly, aluminium in octahedral coordination sites can replace by large ions such as magnesium or iron. Larger cations such as Ca^{2+}, Cs^{+}, K^{+} which are also referred as interlayer cations, can be seen in between layers. Mg^{2+} ions can occupy octahedral coordination places and also in between layers while Ca^{2+} can only occupy in between layers. Therefore, MMT clay has higher potential to intake Mg^{2+} compared to Ca^{2+}. Consequently, the absorption of Mg^{2+} ions increase with an increase in MMT content in the composite.[63]

As there is higher concentration gradient of adsorbent and also large number of vacant sites on the adsorbent, the contact time of the membrane at room temperature in neutral pH, increase the absorption percentage. Once the equilibrium concentration achieved, and all the vacant sites are occupied, adsorption percentage becomes constant. To achieve the equilibrium point, Mg^{2+} ions take approximately 45 minutes while Ca^{2+} take less than 10 minutes. Therefore, it can be concluded, the optimum contact time for the highest absorption of Ca^{2+} and Mg^{2+} ions by the membrane is 45 minutes.

3.4 Characterization of the composites of GO with crosslinked CMC and MMT

3.4.1 FT – IR analysis. According to the FT – IR spectrum of GO-CMC-MMT-3 membrane (Fig. 7a), there are characteristic peaks at 3300 cm^{-1}, 2920 cm^{-1}, 2853 cm^{-1}, 1715 cm^{-1}, 1625 cm^{-1}, 1591 cm^{-1}, 1407 cm^{-1}, 1374 cm^{-1}, 1315 cm^{-1}, 1220 cm^{-1}, 1095 cm^{-1}, 1068 cm^{-1}, 921 cm^{-1}, 894 cm^{-1} and 847 cm^{-1} wave lengths. The FT-IR spectrums of MMT powder, cross linked CMC membrane and Go membrane shows the characteristic peaks of each individual constituent (Fig. 7b).

The broad peak around 3300 cm^{-1} corresponds to the OH^{-} stretching vibrations of H_2O present in GO, CMC, and the interlayer water of MMT particles in the composite. The small peaks at 2920 cm^{-1} and 2853 cm^{-1} arise from the stretching vibrations of $–CH_2–$ groups in the cross-linked CMC structure. The peak at 1715 cm^{-1} represents the protonated carbonyl stretching vibrations of GO and the citric acid component of

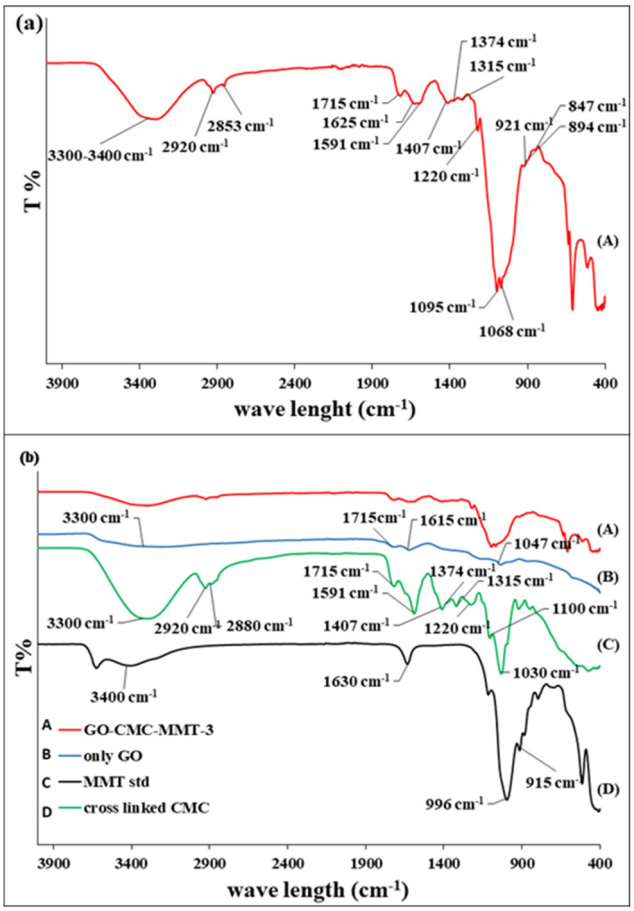

Fig. 7 (a) The expanded FT – IR spectrum of GO-CMC-MMT-3 membrane, (b) the FT – IR spectrums of constituent materials such as GO, MMT powder (MMT std) and cross-linked CMC membrane.

CMC in the composite. Peaks at 1625 cm^{-1} and 1591 cm^{-1} are attributed to carbon–carbon double bonds in GO, H_2O bending vibrations in MMT, and the stretching vibrations of carbonyl groups in CMC, respectively.

Additionally, the peaks at 1407 cm^{-1}, 1374 cm^{-1}, and 1315 cm^{-1} correspond to $-CH_2-$ scissoring and OH^- bending vibrations in CMC particles in the composite membrane.[53,57,58,61] The peaks at 1220 cm^{-1} and 1095 cm^{-1} arise due to vibrations of – C–OH groups in citric acid and epoxy groups in GO. The peaks at the position of 1068 cm^{-1} and 921 cm^{-1} on the composite membrane arise due to –C–O–C– stretching vibrations of CMC matrix and Si–O stretching of MMT particles. Also, there are large number of peaks in the fingerprint region of GO-CMC-MMT-3 membrane due to MMT particles in the composite.[55,58,59,64] These characteristic peaks confirm the effective composite formation from constituent materials.

3.4.2 XRD analysis. According to Fig. 8(a), the GO membrane exhibits characteristic XRD peaks at $2\theta = 9.0°$ (associated with the (002) plane) and 19° (attributed to partially interconnected GO layers *via* oxygen bonds). The cross-linked CMC displays its characteristic XRD peaks at $2\theta = 9.4°$ and $2\theta = 20.1°$. The MMT powder shows distinct peaks at 2θ values of 7.1°, 20°, 28.5°, and 35°.[65,66] In the XRD spectrum of the composite membrane (Fig. 8b), corresponding peaks are observed at 2θ values of 8.06°, 10.6°, 16.46°, 17.84°, and 19.62°. These peaks are generated due to shifting of constituent material peaks to lower 2θ values.

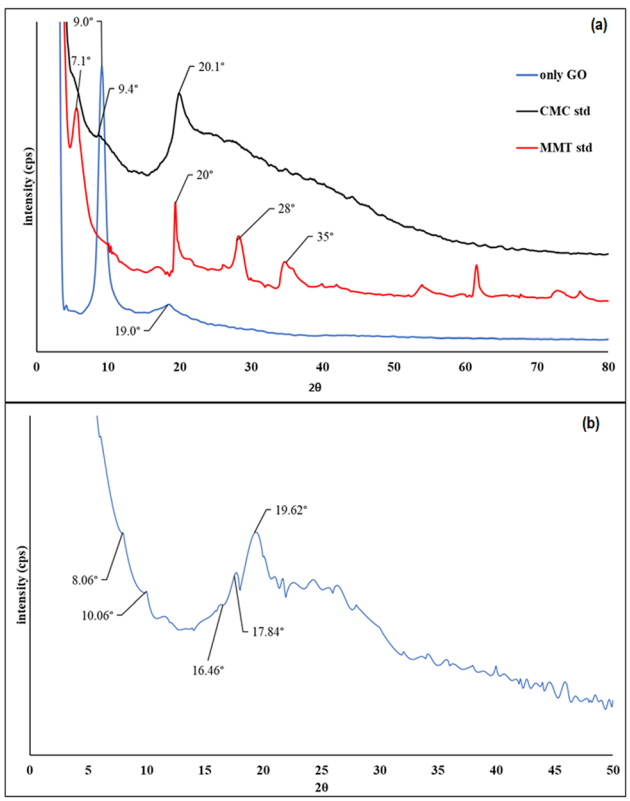

Fig. 8 (a) The XRD spectrums of constituent materials of the GO-CMC-MMT-3 membrane, (b) The XRD spectrum of GO-CMC-MMT-3 membrane.

This shifting result mainly due to increment of interplanar distance of constituent materials during the composite formation. The peak at $2\theta = 8.06°$ in the Fig. 8b, is due to peaks of 7.1° of MMT powder, 9.4° CMC powder, 9.5° of GO after the intercalation.[48] Peak 10.06° in the XRD spectrum of GO-CMC-MMT-3 membrane is due to the shift of 11° peak of MMT clay. Also, the peaks at 16.46°, 17.84°, and 19.62° resulted by the shift of peaks of CMC 20.1° and GO 19°. The shifts in peaks and the presence of characteristic peaks from different constituent materials provide evidence for the successful formation of the nanocomposite with effective intercalation. The peaks at higher 2θ values cannot be distinctly identified, as they represent overlapping from both CMC and MMT.

3.4.3 SEM analysis. The surface morphology and the nature of the CMC-MMT membrane and GO-CMC-MMT-3 membrane were analysed using SEM and obtained images in different magnifications (Fig. 9 and 10). In Fig. 10, CMC-MMT membrane shows MMT particles as big irregular chunks (they are roughly in 1 μm range) and they are embedded in larger matrix of crosslinked CMC polymer (Fig. 9b).

According to the SEM images of GO-CMC-MMT-3 membrane (Fig. 10(a) and (b)), there are clear sheet/layer structures with thickness lower than 100 nm (and roughly in 200–400 nm range

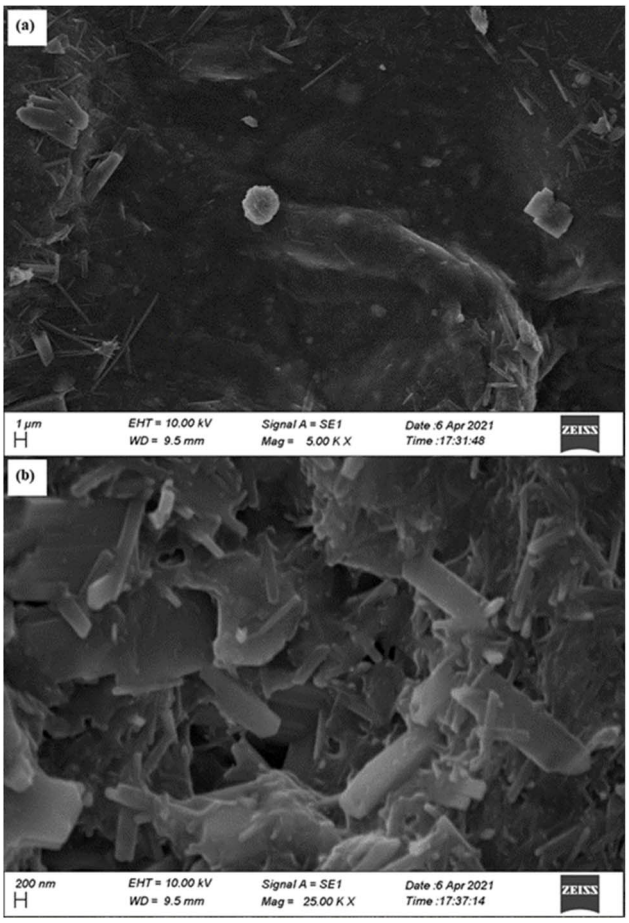

Fig. 9 The SEM images (a) and (b), of CMC-MMT membrane under different magnifications.

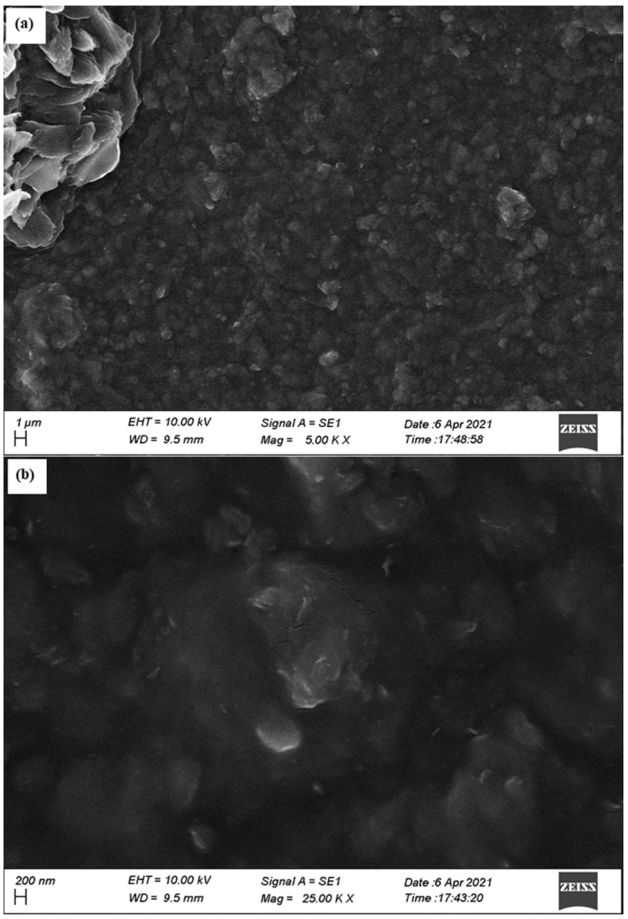

Fig. 10 The SEM images (a) and (b) of GO-CMC-MMT-3 membrane under different magnification.

in length and width), that was not observed in the image of CMC-MMT membrane (Fig. 9). This observation is attributed to the intercalation of GO particles within the GO-CMC-MMT-3 membrane. Additionally, Fig. 9b and 10b clearly show GO particles embedded in the cross-linked CMC membrane.

The SEM images of the nanocomposite provide strong evidence of the successful intercalation and incorporation of GO and MMT particles[67] into the cross-linked CMC polymer matrix.

3.5 Batch adsorption studies

Detailed adsorption studies were conducted to GO-CMC-MMT-3membrane and in the comparative adsorption studies, the contact time was identified as 45 minutes with 53.0% best adsorption percentage for Mg^{2+} and 44.2% for Ca^{2+} (ESI S4†).

3.5.1 The effect of pH on the adsorption. The influence of the pH of the adsorbate solution on the adsorption process was investigated using a pH range of 2 to 8. As shown in Fig. 11, the adsorption percentages of Ca^{2+} and Mg^{2+} varied with pH. Lower pH values resulted in reduced adsorption, likely due to the higher concentration of H^+ ions in the solution. These H^+ ions compete with Ca^{2+} and Mg^{2+} for the available binding sites on the membrane. Additionally, at lower pH levels, the functional

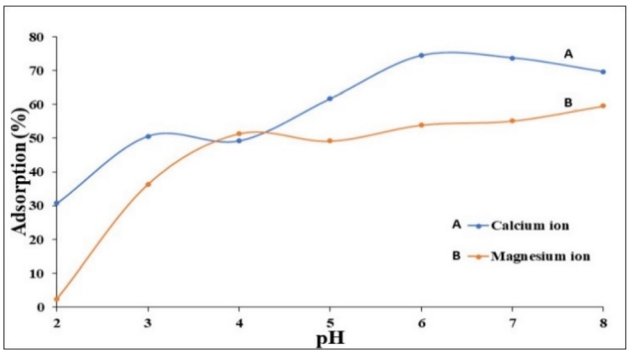

Fig. 11 The changes of the percentage of adsorption for 45 minutes time duration with different pH values.

groups of the composite membrane become protonated, reducing the availability of negative charges on the adsorbent surface. This leads to a decrease in Ca^{2+} and Mg^{2+} adsorption efficiency.[62]

As the pH increases, the competition between Ca^{2+}, Mg^{2+} and H^+ decreases, leading to higher percentage of adsorption. The adsorption percentage increased to its maximum value around pH 6, which is the natural pH of Ca^{2+} and Mg^{2+} solutions. Therefore, the optimal pH range for GO-CMC-MMT-3 membrane is considered to be 6–7. At higher pH values, such as above 8, Ca^{2+} and Mg^{2+} ions tend to precipitate as hydroxides due to their reaction with OH^-. Consequently, the concentration of Ca^{2+} and Mg^{2+} ions decreases at higher pH levels.[62]

3.5.2 Adsorption isotherm studies. Adsorption studies were conducted to identify the most suitable isotherm model for the adsorption process. Results were analysed using Langmuir and Freundlich isotherm models. The determination coefficient of the Langmuir isotherm model was far greater (closer to one) than that of the Freundlich model, which indicated a better fit. This indicates that the Langmuir isotherm model (Fig. S3†) describes adsorption following the formation of a monolayer rather than the Freundlich model. (Fig. S4†). Adsorption constants were calculated using the slope and intercept of respective graphs (Table 1). Accordingly, maximum adsorption capacity was found to be 6.46 mg g^{-1} for Mg^{2+} and 7.98 mg g^{-1} for Ca^{2+}.

Table 1 Calculated Freundlich and Langmuir adsorption isotherm data

Langmuir model					
$C_e/Q_0 = 1/Q_0$. KL + C_e/Q_0					
$y = C + mx$					
Ion	R^2	$1/Q_0$. KL	$1/Q_0$	Q_0 (mg g^{-1})	KL (min^{-1})
Mg^{2+}	0.9802	0.3337	0.1546	6.4683	2.1584
Ca^{2+}	0.9618	0.4998	0.1252	7.9872	3.9920
Freundlich model					
Log Q_e = log K + (1/n) log C_e ($y = C + mx$)					
Ion	R^2	1/n (m)	n	Log k (c)	K (g mg^{-1} min^{-1})
Mg^{2+}	0.7044	0.1399	7.14	0.5680	3.6983
Ca^{2+}	0.9227	0.2700	3.70	0.4574	2.8668

3.5.3 Effect of the temperature (kinetic and thermodynamic study). The kinetic parameters (such as calculated and experimental q_e, K, K_1, R^2) that are obtained according to the graphs of linearized Ho's pseudo second order kinetic equation and linearized Lagergren first order kinetic equation in four different temperatures are given in supportive materials Fig. S5–S12,† also listed in the Table 2.

According to Table 2, the adsorption process of the GO-CMC-MMT-3 membrane shows a higher correlation coefficient (the calculated and experimental q_e are close to each other) with Ho's pseudo second order kinetic model.[65] Therefore, this Ho's pseudo second order kinetic model is the best model to explain adsorption of Ca^{2+} and Mg^{2+} ions on the surface of the nanocomposite GO-CMC-MMT-3. The pseudo-second-order kinetic model is widely regarded as the most suitable model for describing adsorption processes involving chemisorption between the adsorbate and the adsorbent. This suggests that a chemical interaction, such as an exchange or replacement reaction, occurs during the process. In case of replacement, Ca^{2+} and Mg^{2+} ions from the bulk solution can replace the water molecules or H^+ ions on the surface of the nanocomposite.

In addition to that, the effect of temperature on the adsorption rate can be explained by using kinetic data. According to the results, higher adsorption capacity of 13.3 mg g^{-1} exhibit in Mg^{2+} ions at 30 °C, once the nanocomposite reaches its equilibrium capacity after 45 minutes. Even in other temperatures (20 °C, 40 °C, 60 °C) nanocomposite reaches its equilibrium capacity after 45 minutes, but the equilibrium capacity (also highest capacity) gets a lower value (3.7 mg g^{-1}). Same pattern was observed in Ca^{2+} adsorption as well. Ca^{2+} also reached its equilibrium temperature after around 45 minutes with 9.0 mg g^{-1} equilibrium adsorption capacity.[46] The kinetic data clearly demonstrate that the adsorption rate increases with rising temperature. This behaviour can be attributed to the temperature-dependent nature of the rate constant and the activation energy of the adsorption process.

Thermodynamic parameters for the adsorption (Table 3) can be calculated using thermodynamic equations (eqn (5)–(9)) and plots of "ln K_{ap} *vs.* $1/T$" (Arrhenius activation energy plot, (Fig. S13 in ESI†), "ln K_d *vs.* $1/T$" (Van't Hoff plot, Fig. S14 in ESI†). The data indicate that all apparent activation energies for the adsorption processes are positive. As the temperature increases, more adsorbate and adsorbent particles overcome the activation energy barrier, thereby enhancing the reaction rate. As presented in Table 3, the overall standard Gibbs free energy during the adsorption is negative, and that values gradually decrease upon increasing the temperature indicating that the adsorption is more favorable at high temperatures. Therefore, the degree of feasibility of the ion adsorption increases with increasing temperature. Additionally, the negative standard Gibbs free energy values found in the adsorption system indicated that the ion adsorption process is spontaneous. Furthermore, the enthalpy change of the system is also positive, and it indicates the endothermic behavior of the adsorption. The entropy change of the system was positive, and it indicates the randomness at the solid-solution interface increased during the adsorption process.

3.5.4 Reusability study. The reusability of the GO-CMC-MMT-3 membrane was evaluated using solutions of Ca^{2+} and Mg^{2+} ions. As depicted in Fig. S15 in the ESI†, the membrane demonstrated effective performance. Its adsorption capacity was significant during the first two cycles but decreased in subsequent uses. Based on this observation, it can be anticipated that the membrane may be reused once more after reaching saturation. The desorption process, which involves removing Ca^{2+} and Mg^{2+} ions from the membrane surface, was achieved by treating it with a concentrated HCl solution (0.1 mol dm^{-3}).

3.6 Post adsorption studies

3.6.1 Characterization of GO-CMC-MMT-3 membrane after the Ca^{2+} and Mg^{2+} adsorption. The XRD spectrum for Ca^{2+} and Mg^{2+} adsorbed membranes are shown in Fig. S16 in ESI.† According to the spectrum, there is a sharp and high intense peak at $2\theta = 44°$. This sharp peak resulted due to the monolayer of Ca^{2+} and Mg^{2+} on the surface of the nanocomposite and this indicate the successful adsorption of Ca^{2+} and Mg^{2+} by the GO-CMC-MMT-3 membrane.

3.6.2 Gravity filtration. The data concerning gravity filtration, presented in ESI S9,† demonstrates the clear decrease in the concentration of ions in the water sample prepared in the laboratory. It also indicates the stepwise decline in ion concentration with an increasing fraction number, hence showing the saturation of adsorption sites on the adsorbent. On the other hand, in the well water sample, there is no apparent pattern for this decrease in ion concentration. This is due to the

Table 2 Calculated kinetic parameters obtained from graph of linearized Ho's pseudo second order kinetic equation and linearized Lagergren first order kinetic equation in four different temperatures

		Ca^{2+} adsorption				Mg^{2+} adsorption			
		20 °C	30 °C	40 °C	60 °C	20 °C	30 °C	40 °C	60 °C
Experimental q_e		9.50	9.10	8.58	10.07	4.57	13.29	3.66	3.16
GO-CMC-MMT-3 Lagergren first order model	q_e (mg g^{-1})	1.97	2.01	2.57	1.51	1.61	5.32	0.77	0.59
	k_1 (min^{-1})	−0.006	−0.016	−0.010	−0.001	0.003	−0.037	0.004	0.012
	R^2	0.196	0.350	0.219	0.003	0.026	0.974	0.098	0.569
GO-CMC-MMT-3 Ho's pseudo-second-order model	q_e (mg g^{-1})	8.02	9.32	8.52	8.35	2.02	13.77	2.82	1.89
	k_1 (min^{-1})	−0.32	0.03	0.015	−0.093	−0.100	0.017	−0.264	−0.112
	R^2	0.987	0.993	0.872	0.964	0.866	0.994	0.942	0.858

Table 3 The calculated thermodynamic parameters of the adsorption process of the Ca^{2+} and Mg^{2+}

	T (K)	$\Delta G°$ (kJ mol^{-1})	$\Delta H°$ kJ mol^{-1})	$\Delta S°$ (J/K mol)	Activation energy (kJ mol^{-1})
3rd GO/CMC/MMT Ca^{2+} adsorption	293.15	−0.37	6.79	24.50	10.55
	303.15	−0.70			
	313.15	−0.85			
3rd GO/CMC/MMT Mg^{2+} adsorption	293.15	−0.10	6.0	20.88	26.67
	303.15	−0.45			
	313.15	−0.50			

presence of several other cations at moderate concentrations in the ground water, in addition to Ca^{2+} and Mg^{2+}. Hence, the decrease of Ca^{2+} and Mg^{2+} in the well water sample is relatively less and no proper trend can be observed, which is due to the competitiveness of the different cations.

3.7 The mechanism of adsorption

Theoretical adsorption mechanism suggested for Ca^{2+} and Mg^{2+} ions on GO-CMC-MMT-3 membrane surface is supported by adsorption results and characterization. Prepared GO-CMC-MMT-3 membrane bears negative charge in aqueous solutions as a result of a high presence of –OH, –COOH, and epoxy functional groups. The formed negative charge would additionally provide a hindrance against GO layer coagulation owing to the repulsion existing between GO layers in water solutions.

Adsorption of Ca^{2+} and Mg^{2+} ions are influenced by their hydration properties and interaction with the membrane. Ca^{2+} forms a weaker hydration shell than Mg^{2+}, leading to higher adsorption. In contrast, Mg^{2+} has a stronger hydration shell that limits its adsorption. Further membrane hydration also causes to adsorb less hydrated ions like Ca^{2+}. In this situation by adding montmorillonite (MMT) enhances Mg^{2+} adsorption, as Mg^{2+} can occupy both octahedral and interlayer sites in the clay structure, while Ca^{2+} is limited to interlayer sites. Thus, Ca^{2+} shows higher adsorption on the membrane alone, whereas Mg^{2+} adsorption increases when increasing the MMT content.

Apart from that, the overall negative surface charges are normally neutralized by counterions (H^+) or molecules, forming two distinct layers in colloidal chemistry: the inner layer and the diffusion layer. The inner layer consists of a monolayer of counterions, and molecules firmly bound to the surface through chemical interactions and can be considered as an inherent part of the nanocomposite surface.

The counter ions in the diffusion layer are loosely associated with the surface by Coulomb interactions and actively exchangeable with ions from the bulk solution depending on the concentration gradient. This major mechanism was used in this study to remove Ca^{2+} and Mg^{2+} ions from the bulk solution.[68]

4 Conclusions

This study was primarily focused on the development of a nanocomposite of graphene oxide (GO) and biopolymers, for effective reduction of water hardness. Based on solubility studies and comparative adsorption studies of calcium (Ca^{2+}) and magnesium (Mg^{2+}) ions, the GO-CMC-MMT-3 composite prepared from graphene oxide, cross-linked carboxymethyl cellulose (CMC), and montmorillonite (MMT) was found to be the most effective material. The effectiveness of its synthesis was confirmed by characterization methods such as X-ray diffraction (XRD), Fourier-transform infrared spectroscopy (FT-IR), scanning electron microscopy (SEM), and UV-visible spectroscopy.

The important parameters that would influence the adsorption process, including optimal pH and contact time, were studied. Accordingly, it was found that the optimal pH for both Ca^{2+} and Mg^{2+} ions is at around pH 6–7, while the optimal contact time is 45 minutes. Thermodynamic analysis depicts that the adsorption process is endothermic and less spontaneous. Reusability studies showed the nanocomposite membrane was efficient for reuse up to two cycles. At the same time satisfactory results were given by the gravity filtration study. Therefore, based on these findings, it can be concluded that the prepared GO-CMC-MMT-3 nanocomposite is a potential adsorbent for the removal of Ca^{2+} and Mg^{2+} ions from hard water.

Data availability

All data have been presented in the manuscript. Other data are represented in the ESI.† Any raw data can be provided on request.

Conflicts of interest

There are no conflicts of interest to declare.

Acknowledgements

Authors like to express their sincere gratitude to the National Research Council for funding water purification projects of CAMD (Grant No. NRC TO 16-018).

Notes and references

1 Y. Takahashi and Y. Imaizumi, *Eisei kagaku*, 1988, **34**, 475–479.
2 S. Wickramarathna, S. Balasooriya, S. Diyabalanage and R. Chandrajith, *J. Trace Elem. Med. Biol.*, 2017, **44**, 298–306.
3 S. J. Wimalawansa, *J. Environ. Health Sci. Eng.*, 2016, **2**, 1–11.
4 P. Sengupta, *Int. J. Prev. Med.*, 2013, **4**, 866–875.
5 R. E. Thompson, *Can. J. public helth*, 2014, **23**, 507–516.

6 S. A. Greeley and E. Bartow, *J.–Am. Water Works Assoc.*, 1916, **3**, 142–162.
7 G. C. Baker, *J. - Am. Water Works Assoc.*, 1924, **11**, 128–149.
8 M. K. Ahn, R. Chilakala, C. Han and T. Thenepalli, *Water*, 2018, **10**, 1–10.
9 E. Helmy and M. Hussein, *Ijcbs*, 2017, **12**, 1.
10 Z. Y. Leong and H. Y. Yang, *ACS Omega*, 2020, **5**, 2097–2106.
11 Y. Yu, H. Jin, X. Jin, R. Yan, L. Zhang and X. Chen, *Ind. Eng. Chem. Res.*, 2018, **57**, 6585–6593.
12 Z. Yu, T. Qi, J. Qu, L. Wang and J. Chu, *J. Hazard. Mater.*, 2009, **167**, 406–412.
13 M. Şahin, H. Görçay, E. Kir and Y. Şahin, *React. Funct. Polym.*, 2009, **69**, 673–680.
14 M. H. Entezari and M. Tahmasbi, *Ultrason. Sonochem.*, 2009, **16**, 356–360.
15 A. H. Mahvi, F. Shafiee and K. Naddafi, *Int. J. Environ. Sci. Technol.*, 2005, **1**, 301–304.
16 N. Kabay, M. Demircioglu, E. Ersöz and I. Kurucaovali, *Desalination*, 2002, **149**, 343–349.
17 S. C. Low, C. Liping and L. S. Hee, *Desalination*, 2008, **221**, 168–173.
18 M. Shareef, A. S. M. Kamdod and A. B. Mohammed, *Iarjset*, 2015, **2**, 83–84.
19 L. Fu, J. Wang and Y. Su, *Sep. Purif. Technol.*, 2009, **68**, 390–396.
20 S. Mopoung and T. Bunterm, *Carbon:Sci. Technol.*, 2016, **8**, 13–19.
21 B. T. Perera, R. M. H. Rajapaksha, R. C. W. Arachchige and I. R. M. Kottegoda, *Int. J. Chem. Sci.*, 2020, **4**, 22–27.
22 C. Rolence, *Int. J. Sci. Technol. Soc.*, 2014, **2**, 97.
23 M. S. Fernando, W. R. M. De Silva and K. M. N. De Silva, *Int. J. Nanosci.*, 2014, **13**(4), 1440002.
24 D. Kannan and N. Mani, *Int. J. Pharma Sci. Res.*, 2015, **6**, 374–381.
25 E. Hettiarachchi, N. Kottegoda and A. D. L. Chandani Perera, *Desalin. Water Treat.*, 2017, **66**, 103–110.
26 J. John and M. C. Nwonu, *Int. Digit. Organ. Sci. Res.*, 2019, **4**, 84–90.
27 A. M. Saeed and M. J. Hamzah, *Int. J. Adv. Biol. Biomed. Res.*, 2013, **1**, 1142–1156.
28 M. N. Sepehr, M. Zarrabi, H. Kazemian, A. Amrane, K. Yaghmaian and H. R. Ghaffari, *Appl. Surf. Sci.*, 2013, **274**, 295–305.
29 K. Thongdee, K. Parun, S. Benjatitmongkhon, K. Jamtim and S. Mopoung, *Am. J. Appl. Sci.*, 2017, **14**, 636–648.
30 A. Mohamed Gad, *SDRP J. Earth Sci. Environ. Stud.*, 2016, **1**, 109–119.
31 M. Said, A. Alawad and I. J. Humanit, *Soc. Sci. Educ.*, 2018, **5**, 11–15.
32 G. Cetin, *ISRN Anal. Chem.*, 2014, **2014**, 1–7.
33 P. Pentamwa, W. Thipthara and S. Nuangon, *Int. J. Environ. Sci. Dev.*, 2011, **2**, 479–482.
34 M. A. Tofighy and T. Mohammadi, *Desalination*, 2011, **268**, 208–213.
35 M. Fathy, T. Abdel Moghny, M. A. Mousa, A. H. A. A. El-Bellihi and A. E. Awadallah, *Appl. Nanosci.*, 2016, **6**, 1105–1117.
36 S. J. Choi, *Clays Clay Miner.*, 2019, **67**, 91–98.
37 S. Gurunathan, M. A. Iqbal, M. Qasim, C. H. Park, H. Yoo, J. H. Hwang, S. J. Uhm, H. Song, C. Park, J. T. Do, Y. Choi, J. H. Kim and K. Hong, *Nanomaterials*, 2019, **9**(7), 969.
38 X. Gao, Y. Hu, T. Guo, X. Ye, Q. Li, M. Guo, H. Liu and Z. Wu, *Adsorpt. Sci. Technol.*, 2013, **31**, 45–58.
39 J. Fan, C. D. Grande and D. F. Rodrigues, *Environ. Sci.:Nano*, 2017, **4**, 1808–1816.
40 B. Anegbe, I. H. Ifijen, M. Maliki, I. E. Uwidia and A. I. Aigbodion, *Environ. Sci. Eur.*, 2024, **36**, 15.
41 D. S. Lakshmi, N. Trivedi and C. R. K. Reddy, *Carbohydr. Polym.*, 2017, **157**, 1604–1610.
42 J. M. T. Ayrat Dimiev, D. V. Kosynkin, L. B. Alemany and P. Chaguine, *J. Am. Chem. Soc.*, 2012, 2815–2822.
43 E. A. Shalaby, in *Biological Activities and Application of Marine Polysaccharides*, ed. P. Nechita, InTech, Croatia, 1st edn, 2017, pp. 209–227.
44 A. Spoială, C. I. Ilie, D. Ficai, A. Ficai and E. Andronescu, *Materials*, 2021, **14**, 1–29.
45 W. Wei, S. Kim, M. H. Song, J. K. Bediako and Y. S. Yun, *J. Taiwan Inst. Chem. Eng.*, 2015, **57**, 104–110.
46 A. K. D. V. K. Wimalasiri, M. S. Fernando, K. Dziemidowicz, G. R. Williams, K. R. Koswattage, D. P. Dissanayake, K. M. N. De Silva and R. M. De Silva, *ACS Omega*, 2021, **6**, 13527–13543.
47 H. F. Heiba, A. A. Taha, A. R. Mostafa, L. A. Mohamed and M. A. Fahmy, *Korean J. Chem. Eng.*, 2018, **35**, 1844–1853.
48 G. Thakur, A. Singh and I. Singh, *Sci. Pharm.*, 2016, **84**, 603–617.
49 J. Fawaz and V. Mittal, in *Synthesis Techniques for Polymer Nanocomposite*, ed. V. Mittal, Wiley-VCH Verlag GmbH & Co. KGaA, Weinheim, 1st edn, 2015, pp. 1–30.
50 P. H. C. Camargo, K. G. Satyanarayana and F. Wypych, *Mater. Res.*, 2009, **12**, 1–39.
51 H. L. Poh, F. Šaněk, A. Ambrosi, G. Zhao, Z. Sofer and M. Pumera, *Nanoscale*, 2012, **4**, 3515–3522.
52 J. Chen, B. Yao, C. Li and G. Shi, *Carbon*, 2013, **64**, 225–229.
53 J. S. Piccin, G. L. Dotto and L. A. A. Pinto, *Braz. J. Chem. Eng.*, 2011, **28**, 295–304.
54 N. Ghasemi, P. Tamri, A. Khademi, N. S. Nezhad and S. R. W. Alwi, *IERI Procedia*, 2013, **5**, 232–237.
55 D. Khalili, *New J. Chem.*, 2016, **40**, 2547–2553.
56 J. L. S. Gascho, S. F. Costa, A. A. C. Recco and S. H. Pezzin, *J. Nanomater.*, 2019, **2019**, 12–16.
57 L. Stobinski, B. Lesiak, A. Malolepszy, M. Mazurkiewicz, B. Mierzwa, J. Zemek, P. Jiricek and I. Bieloshapka, *J. Electron Spectrosc. Relat. Phenom.*, 2014, **195**, 145–154.
58 K. Wilpiszewska, A. K. Antosik, B. Schmidt, J. Janik and J. Rokicka, *Polymers*, 2020, **12**, 1–16.
59 M. I. H. Mondal, M. S. Yeasmin and M. S. Rahman, *Int. J. Biol. Macromol.*, 2015, **79**, 144–150.
60 G. T. D. Chandrakumara, D. M. S. N. Dissanayake, M. M. M. G. P. G. Mantilaka, R. T. De Silva, H. M. T. G. A. Pitawala and K. M. N. De Silva, *J. Nanomater.*, 2019, **2019**, 1049142.
61 Y. Sakai, K. Hayano, H. Yoshioka and H. Yoshioka, *Polym. J.*, 2001, **33**, 640–642.

62 S. Es, M. Fathy, E. Im, A. Sa, N. Shehata and S. Am, *Int. J. Chem. Sci. Res.*, 2018, **16**, 1–11.
63 M. Norsuzila Ya'acob, M. Abdullah, M. Ismail, M. Medina, T. L. Talarico, I. A. Casas, T. C. Chung, W. J. Dobrogosz, L. Axelsson, S. E. Lindgren, W. J. Dobrogosz, L. Kerkeni, P. Ruano, L. L. Delgado, S. Picco, L. Villegas, F. Tonelli, M. Merlo, J. Rigau, D. Diaz and M. Masuelli, *Intech*, 1989, **32**, 137–144.
64 M. Alshabanat, A. Al-Arrash and W. Mekhamer, *J. Nanomater.*, 2013, **2013**, 650725.
65 R. Siburian, H. Sihotang, S. Lumban Raja, M. Supeno and C. Simanjuntak, *Orient. J. Chem.*, 2018, **34**, 182–187.
66 A. Abdel-Galil, H. E. Ali, A. Atta and M. R. Balboul, *J. Radiat. Res. Appl. Sci.*, 2014, **7**, 36–43.
67 X. Hao, S. Yang, T. E, L. Liu, D. Ma and Y. Li, *J. Alloys Compd.*, 2022, **923**, 1–38.
68 A. M. Dimiev, L. B. Alemany and J. M. Tour, *ACS Nano*, 2013, **7**, 576–588.